batteries

MDPI

Article

In Situ/Operando Techniques for Unraveling Mechanisms of Ionic Transport in Solid-State Lithium Indium Halide Electrolyte

Farzaneh Bahmani [1], Collin Rodmyre [1], Karen Ly [1], Paul Mack [2] and Alevtina White Smirnova [1,3,*]

[1] Materials Engineering and Science Program, South Dakota Mines, Rapid City, SD 57701, USA; farzaneh.bahmani@mines.sdsmt.edu (F.B.)
[2] Thermo Fisher Scientific, East Grinstead RH19 1UB, West Sussex, UK
[3] Department of Chemistry, Biology, and Health Sciences, South Dakota Mines, Rapid City, SD 57701, USA
* Correspondence: alevtina.smirnova@sdsmt.edu

Abstract: Over the past years, lithium-ion solid-state batteries have demonstrated significant advancements regarding such properties as safety, long-term endurance, and energy density. Solid-state electrolytes based on lithium halides offer new opportunities due to their unique features such as a broad electrochemical stability window, high lithium-ion conductivity, and elasticity at close to melting point temperatures that could enhance lithium-ion transport at interfaces. A comparative study of lithium indium halide (Li_3InCl_6) electrolytes synthesized through a mechano-thermal method with varying optimization parameters revealed a significant effect of temperature and pressure on lithium-ion transport. An analysis of Electrochemical Impedance Spectroscopy (EIS) data within the temperature range of 25–100 °C revealed that the optimized Li_3InCl_6 electrolyte reveals high ionic conductivity, reaching 1.0 mS cm^{-1} at room temperature. Herein, we present the utilization of in situ/operando X-ray Photoelectron Spectroscopy (XPS) and in situ X-ray powder diffraction (XRD) to investigate the temperature-dependent behavior of the Li_3InCl_6 electrolyte. Confirmed by these methods, significant changes in the Li_3InCl_6 ionic conductivity at 70 °C were observed due to phase transformation. The observed behavior provides critical information for practical applications of the Li_3InCl_6 solid-state electrolyte in a broad temperature range, contributing to the enhancement of lithium-ion solid-state batteries through their improved morphology, chemical interactions, and structural integrity.

Keywords: solid-state batteries; lithium halides; temperature; pressure; in situ XRD and XPS

Citation: Bahmani, F.; Rodmyre, C.; Ly, K.; Mack, P.; White Smirnova, A. In Situ/Operando Techniques for Unraveling Mechanisms of Ionic Transport in Solid-State Lithium Indium Halide Electrolyte. *Batteries* **2024**, *10*, 21. https://doi.org/10.3390/batteries10010021

Academic Editor: Hirotoshi Yamada

Received: 29 November 2023
Revised: 30 December 2023
Accepted: 31 December 2023
Published: 5 January 2024

1. Introduction

The increasing demand for clean energy storage systems and the swift growth of the electric vehicle industry have highlighted the safety concerns associated with conventional liquid lithium-ion batteries. These batteries use flammable liquid electrolytes and are susceptible to thermal runaway [1,2]. In contrast, solid-state batteries (SSBs) with solid-state electrolytes (SSEs) have captured significant attention for their inherent non-flammable nature and safety [3,4]. Additionally, SSEs enable the use of a lithium metal anode, greatly enhancing the energy density of a battery to meet the rising demand for high-performance energy storage systems [5,6]. However, further research is needed to address the challenges associated with their development and ensure their widespread commercialization. An essential aspect in this pursuit is the identification of highly conductive solid-state electrolytes possessing both high lithium-ion conductivity and electrochemical stability that are crucial for safe and energy-dense SSBs [7]. Current research in SSEs is predominantly focused on sulfide-based and oxide-based SSEs. Sulfide SSEs typically display substantial ionic conductivity (10^{-3} to 10^{-4} S·cm^{-1}) at room temperature, along with good thermal stability and a broad electrochemical stability window [8]. However, these electrolytes are extremely sensitive to the ambient environment, readily reacting with water and oxygen to produce

toxic H_2S gas [9]. Furthermore, direct contact between sulfur-based SSEs and cathodes results in substantial interfacial resistance due to side reactions, which are exacerbated by the decomposition of sulfide electrolytes at high voltages. Specifically, oxidation of the sulfur-based Li_6PS_5Cl electrolyte at the interface with positive electrode materials, such as $LiCoO_2$, $LiNi_{1/3}Co_{1/3}Mn_{1/3}O_2$, and $LiMn_2O_4$, leads to the formation of elemental sulfur, lithium polysulfides, P_2S_x ($x \geq 5$), phosphates, and LiCl with low ionic and electronic conductivity [10].

In contrast to sulfur-based SSEs, oxide-based solid electrolytes are air-stable but demonstrate high resistances at electrolyte–cathode interfaces [11–13]. Furthermore, their synthesis involves high-temperature sintering, which causes side reactions between the electrode and oxide SSEs during the co-sintering step [11]. These unfavorable factors have hindered further developments in oxide SSEs. To address these challenges, researchers have made notable advancements in the development of halide-based SSEs. Lithium halide electrolytes hold great promise regarding their high ionic conductivity, thermal stability, and wide electrochemical stability window above 4.0 V [14,15]. For example, $LiInI_4$ electrolytes show an ionic conductivity of 10^{-8} S·cm^{-1} at 25 °C [16]. An ionic conductivity of $2{\cdot}10^{-5}$ S·cm^{-1} is reported for $Li_2Ba_{0.5}InBr_6$ [17]. Unfortunately, most of the reported halide-based electrolytes demonstrate relatively low ionic conductivity: typically, around 10^{-4} S·cm^{-1} even at high temperatures [15]. In comparison, a Li_3InCl_6 solid-state electrolyte demonstrates high ionic conductivity and compatibility with high-voltage cathode materials such as $LiCoO_2$ and $LiNi_{0.8}Co_{0.1}Mn_{0.1}O_2$ (NCM) [18]. A reversible areal capacity of 12.16 mAh·cm^{-2} at 0.1 mA for the NMC811/Li_3InCl_6/$Li_{10}GeP_2S_{12}$/In electrochemical cell at room temperature [19] and specific capacity of 127 mAh·g^{-1} at 0.1C-rate for the LiCoO $_2$–Li_3InCl_6/Li_3InCl_6/In cell [15] were reported. A notable limitation of halide-based electrolytes is their sensitivity to moisture [15], which in the case of Li_3InCl_6, triggers side reactions leading to lower ionic conductivity [20]. As well as moisture, the influence of operating temperature on the ionic conductivity of halide-based electrolytes is a critical factor for practical applications. However, to the best of our knowledge, no studies are exploring the temperature effect on the structure, composition, and chemical stability of Li_3InCl_6 solid-state electrolytes.

This study describes an optimized solid-state mechano-thermal method for the synthesis of Li_3InCl_6 powder, utilizing different ball-milling times and annealing temperatures. A comprehensive investigation of the Li_3InCl_6 ionic conductivity with temperature provides a unique picture of the material's behavior that was acquired by using in situ XRD for tracking phase transformations and in situ XPS to monitor the chemical changes. The properties of the electrolyte pellets fabricated from the synthesized Li_3InCl_6 powder were investigated under varying pressures, which proves to be a critical factor in achieving high lithium-ion conductivity at room temperature. Additional information regarding the Li_3InCl_6 behavior over a wider temperature range was acquired from the thermogravimetric analysis with differential scanning calorimetry (TGA/DSC). By investigating the temperature-dependent behavior of Li_3InCl_6 SSEs, the phase transformations of Li_3InCl_6 were revealed, providing a path forward to further improvements in lithium-ion conductivity at room temperature.

2. Materials and Methods

2.1. Synthesis of Li_3InCl_6 Solid-State Electrolyte

The Li_3InCl_6 inorganic precursors, specifically LiCl (99.95%, Cat. number 916013 Sigma-Aldrich, USA) and $InCl_3$ (99.999%, Cat. number 011856.18, Thermo Fisher Scientific, USA), with a stoichiometric ratio of 3:1, were mixed and ground using agate mortar and pestle, and then mechanically mixed for 12 or 24 h using a high-energy ball mill at 600 rpm (Table 1). The ball-milled precursors were placed in a Schlenk tube inside the argon glovebox to prevent moisture absorption. Subsequently, the sealed tube was placed in the tubular furnace. The samples were annealed at different temperatures (260, 450, 500, or 600 °C) for 2 or 5 h at a heating rate of 5 °C min^{-1} in a vacuum, using the vacuum pump with a suction power of 2.5 ft^3 min^{-1}.

Table 1. Experimental conditions for the synthesis of Li_3InCl_6 solid-state electrolyte.

Experiment Number	Ball-Milling Duration (h)	Annealing Temperature (°C)	Annealing Time (h)
1	12	-	-
2	24	600	5
3	24	500	5
4	24	450	5
5	12	450	5
6	12	260	2

2.2. Materials' Characterization

The morphology, structure, and chemical composition of the synthesized powders and compressed Li_3InCl_6 samples were characterized by scanning electron microscopy (SEM) using DualBeam Helios 5CX from ThermoFisher Scientific, USA, quipped with the EDX analyzer.

In situ XRD analysis was performed using the EMPYREAN X-ray diffractometer from Malvern PANalytical, USA (Co Kα λ = λ = 1.78899 Å) in the temperature range of 25–280 °C. For these measurements, a Li_3InCl_6 pellet made under a pressure of 280 MPa was placed in an air-tight sample holder inside an argon glovebox and transferred to the diffractometer. The resulting non-ambient datasets were analyzed using Malvern PANalytical's High Score software v5.2.

In situ/operando X-ray Photoelectron Spectroscopy (XPS) data were obtained from the Thermo Fisher Scientific Nexsa G2 surface analysis system. The analysis was performed with monochromated aluminum K-alpha emission, employing a photon energy of 1486 eV. The Li_3InCl_6 powder samples were loaded into the Vacuum Transfer Module (VTM) followed by XPS data acquisition. The atomic percent (at. %) values of the elements detected on the surface of the Li_3InCl_6 particles were calculated from the observed intensities of the XPS peaks (peak areas above an interpolated background), which were then normalized for photoionization cross-section for each element.

The water absorption behavior of Li_3InCl_6 was evaluated by using a TGA/DSC measurement. The samples (7.06 mg) were weighed in the argon glove box and transferred in a sealed container to the SDT Q600 V20.9 Build 20 analyzer. The powder sample was moved into an alumina pan and placed in the analysis chamber. The measurements were conducted under a flowing argon gas (100 mL min^{-1}) in the temperature range of 25 to 600 °C at a scan rate of 5 °C min^{-1}.

2.3. Electrochemical Characterization

The ionic conductivity of Li_3InCl_6 was measured by the Solartron 1260 analyzer in the frequency range from 0.3 MHz to 1.0 Hz and temperatures from 25 to 100 °C. For each EIS measurement, a powder sample was placed within a 12 mm diameter PEEK split cell from MSE supplies equipped with two stainless steel electrodes, a pressure device, and a load sensor. The thickness of the pellet was between 0.5 and 0.8 mm depending on the amount of pressure used. The solid-state electrolyte disks from the optimized Li_3InCl_6 powder (Table 1, sample 6) were produced by applying different compression forces: specifically, 216, 260, and 286 MPa (2.5, 3, and 3.3 tons, respectively). The ionic conductivity was determined using the following equation: $\sigma = L/RS$, where L is a post-palletization thickness (cm), S is the pellet area (cm^2), and R is the resistance (Ω). The activation energy (E_a) was derived from the corresponding ionic conductivity plots (log σ vs. 1/T).

3. Results and Discussion

3.1. Structural and Thermal Analysis

The X-ray diffraction (XRD) patterns of the ball-milled and annealed Li_3InCl_6 samples (Table 1) reveal a change in crystallinity based on the annealing temperatures (Figure 1a). Without heat treatment, the sample ball milled for 12 h exhibited broad peaks indicating

its low crystallinity. In contrast, all the samples heat-treated in the temperature range of 260–600 °C revealed sharp peaks and high crystallinity, which correlates with earlier publication [15]. At lower annealing temperatures (260–450 °C), the XRD spectra matched the monoclinic Li_3InCl_6 crystal structure belonging to the C2/m space group (ICCD No. 04-009-9027). However, at higher annealing temperatures (500 and 600 °C), certain characteristic peaks of Li_3InCl_6 at approximately 2θ = 21° and 25° were absent. In particular, the XRD pattern of the Li_3InCl_6 sample annealed at 600 °C revealed the presence of an impurity phase, specifically InOCl (2θ = 12.5°) [21]. In addition, a weak unknown peak (2θ = 15.2°) was observed at 500 °C, which diminished as the annealing temperature was decreased to 260 °C.

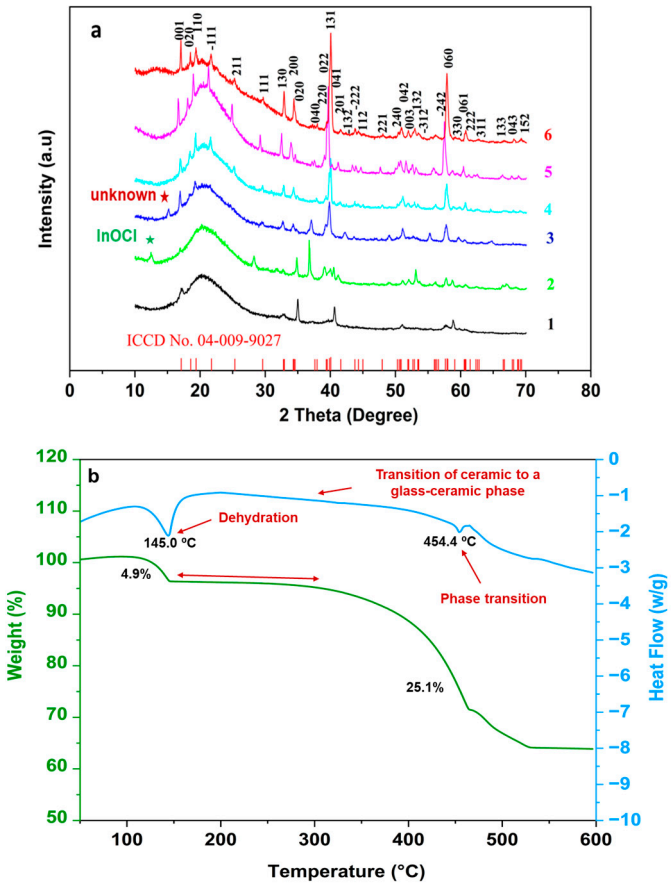

Figure 1. X-ray diffraction patterns of the ball-milled and annealed Li_3InCl_6 samples, alongside the standard pattern of reported Li_3InCl_6 (ICSD No. 04-009-9027) (**a**). Data from the TGA/DSC analysis of the optimized Li_3InCl_6 sample (Table 1, Sample 6) (**b**).

Based on the XRD data, it was concluded that a high-purity Li_3InCl_6 solid electrolyte can be produced at low annealing temperatures (260 °C) and relatively short ball-milling times (12 h). Compared to previous reports where Li_3InCl_6 powders usually required 24 h of ball milling [15], the Li_3InCl_6 samples selected in this study for electrochemical studies were synthesized at a much lower temperature of 260 °C (Table 1, Sample 6).

An important property of many solid-state electrolytes and, specifically, indium halides is moisture sensitivity [19]. The synthesized Li_3InCl_6 samples demonstrated moisture sensitivity, which was observed through controlled exposure to ambient air, leading to the formation of $Li_3InCl_6{\cdot}2H_2O$ [22]. Figure 1b illustrates semi-quantitative TGA/DSC data for the optimized Li_3InCl_6. The weight loss of the Li_3InCl_6 sample at 145.0 °C is 4.91%, signifying the removal of the water molecules from the Li_3InCl_6 surface and producing an endothermic effect. It was observed that at higher temperatures (145 to 280 °C), the mass of the Li_3InCl_6 sample remains constant. However, the endothermic effect observed

in this temperature range could be assigned to a partial and gradual transformation from a ceramic to a glass–ceramic phase, which was observed earlier in argyrodite [23] and lithium oxyhalide [24] solid-state electrolytes. At 454.4 °C, the third endothermic effect is observed, which could be explained by the phase transition. This observation provides essential insights into the material's dynamic behavior under thermal conditions.

3.2. Morphological Analysis

Material morphology is vital for shaping properties and influencing material properties. Based on the results of the comparative study, the morphology of the Li_3InCl_6 electrolyte powder was studied at different magnifications (Figure 2a–c). The Li_3InCl_6 particles exhibit characteristic agglomerate morphology consisting of smaller particles of irregular shape. Their particle size ranges from 200 nm to 500 nm, which offers greater flexibility to tolerate the volume expansion during charge–discharge processes, lower porosity after applying compression force, and better interfacial contact with cathode nanoparticles. The elemental analysis of Li_3InCl_6 nanostructures performed by EDS revealed the Li_3InCl_6 chemical composition and uniform distribution of In and Cl with the atomic ratio of In (at. %):Cl (t. %) = 1:5.9 that matches the atomic ratio of these elements in Li_3InCl_6 (Figure 2c,d).

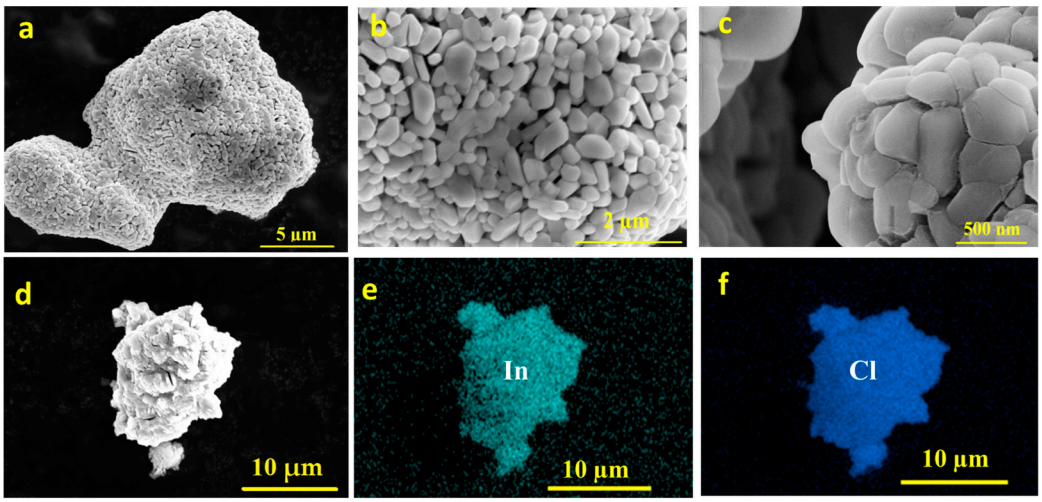

Figure 2. SEM images of the optimized Li_3InCl_6 electrolyte at different magnifications (**a**–**c**); backscattered image (**d**); and EDS X-ray maps of indium and chloride (**e**,**f**).

3.3. Electrochemical Performance Evaluation

The ionic conductivity of the optimized Li_3InCl_6 sample was evaluated by investigating the impact of the compression force applied to the synthesized powder and by changing the temperature. The Nyquist plots (Figure 3a–c) depict the Li_3InCl_6 sample's behavior under pressures ranging from 216 to 286 MPa and temperatures changing from 25 °C to 100 °C in symmetrical cells with stainless steel blocking electrodes. The calculated ionic conductivities are represented by ionic conductivity plots (Figure 3d–f). Notably, the sample's resistivity at room temperature decreased from 105 Ω at 216 MPa to 45 Ω at 286 MPa, which corresponds to ionic conductivities of 0.42 mS/cm and 1.0 mS/cm, respectively. These data align favorably with the previously published results for Li_3InCl_6 synthesized from water solutions [25].

It was observed that the activation energy for the lithium-ion transfer in Li_3InCl_6 increases significantly with both temperature and the applied compression force. Specifically, within the temperature range of 25–70 °C and compression forces of 216, 260, and 286 MPa, the corresponding values of activation energy decreased from 0.135 to 0.116, and 0.111 eV, respectively. This result can be attributed to pressure-induced modification in grain-to-grain contacts, which is further illustrated in Figure 4. As depicted in Figure 3d–f, ionic conductivity plots consist of two fitting lines from 25 to 60 °C and 70 to 100 °C. As the

temperature increases, the slope of the ionic conductivity plot becomes steeper above 70 °C, indicating a higher lithium-ion diffusion and activation energy for lithium-ion transport. This result could be explained by the transformations of the Li_3InCl_6 monoclinic structure at higher temperatures leading to a significant conductivity increase at and above 70 °C. In the past, similar observations were reported for chlorine-based electrolytes that demonstrated orthorhombic to tetragonal/cubic phase transformations [26]. Another possible explanation for the observed increase in lithium-ion conductivity could be attributed to the decrease in the interfacial barrier at the solid electrolyte interface (SEI) at elevated temperatures [26]. These assumptions were further tested by SEM, in situ XRD, and XPS analysis.

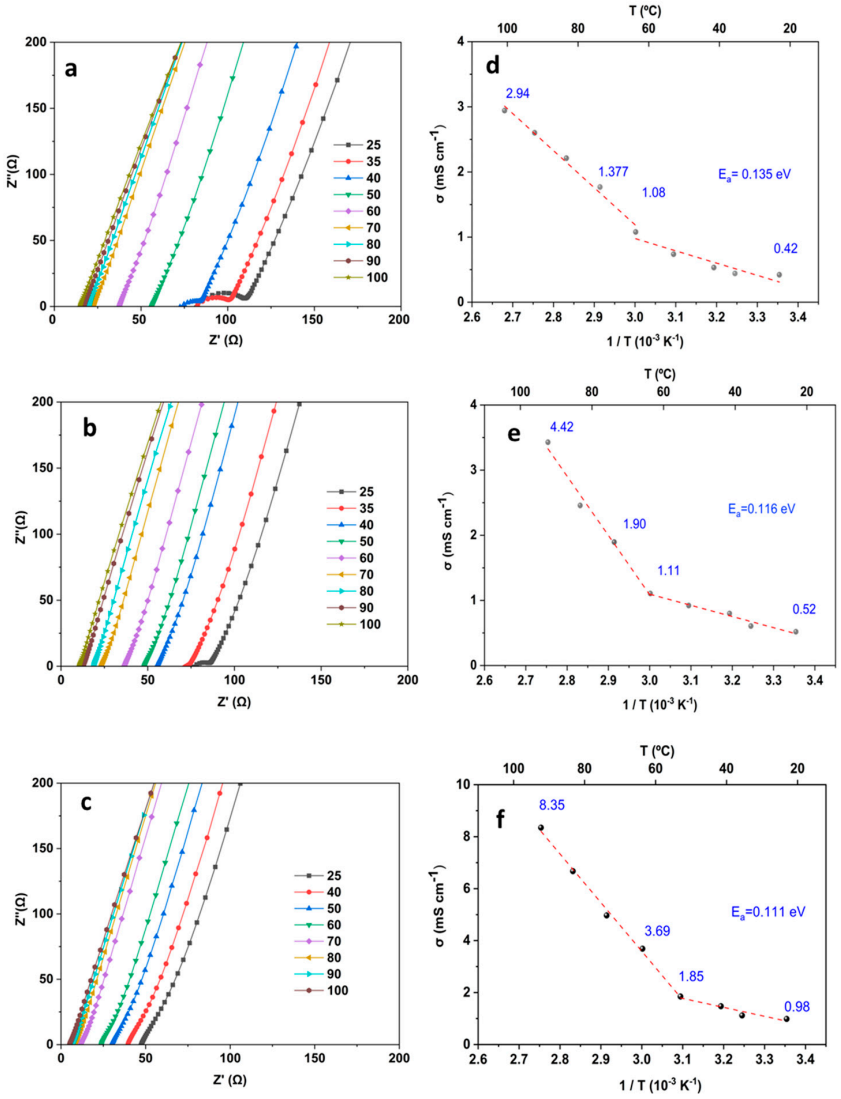

Figure 3. The EIS data for Li_3InCl_6 electrolyte at different compressions in the temperature range (**a**–**c**). The ionic conductivity plots for the Li_3InCl_6 solid-state electrolyte in the temperature range with different pressures demonstrate a visible phase transition at 70 °C (**d**–**f**). Note: the results in a and d were produced at 216 MPa; (**b**,**e**)—at 260 MPa; and (**c**,**f**)—at 286 MPa.

The effect of compression force on the morphology of Li_3InCl_6 pellets and its correlation with observed changes in lithium-ion conductivity were studied by SEM (Figure 4a–c). At a lower compression force of 216 MPa, the surface of the pellet is less uniform and shows more voids within the structure, yielding lower conductivity. Conversely, higher compression results in higher ionic conductivity due to an increased material density and more uniform morphology, fostering increased contact between grains [27].

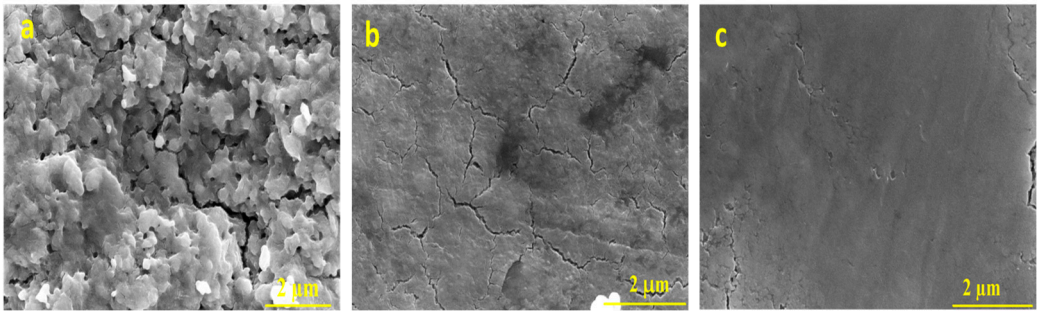

Figure 4. SEM images of the pellet surface under different compression forces of 216 MPa (**a**); 260 MPa (**b**); and 286 MPa (**c**).

3.4. In Situ XRD and XPS Analysis

In situ XRD analysis for the optimized Li_3InCl_6 electrolyte was performed by using a temperature-programmed heating method in the temperature range from 25 °C to 280 °C (Figure 5a–d). The observed peaks at 2θ = 32.7.8°, 34.3°, 51.2°, 57.7°, and 59.6° demonstrate a gradual shift toward lower 2θ values within the temperature range of 70 °C to 280 °C, which correlates with the change in activation energy for lithium-ion transport at 70 °C (Figure 3d–f). These results are further confirmed by the XRD spectrum at 70 °C and higher, which shows a new shoulder peak at 2θ = 39.3°, indicating the formation of a modified crystal structure. Moreover, below 200 °C, the peaks at 2θ = 37.1°, 42.2°, and 55.1° exhibit higher intensities (Figure 5c,d). As the temperature surpasses 200 °C, these peaks diminish, implying an ongoing transformation process.

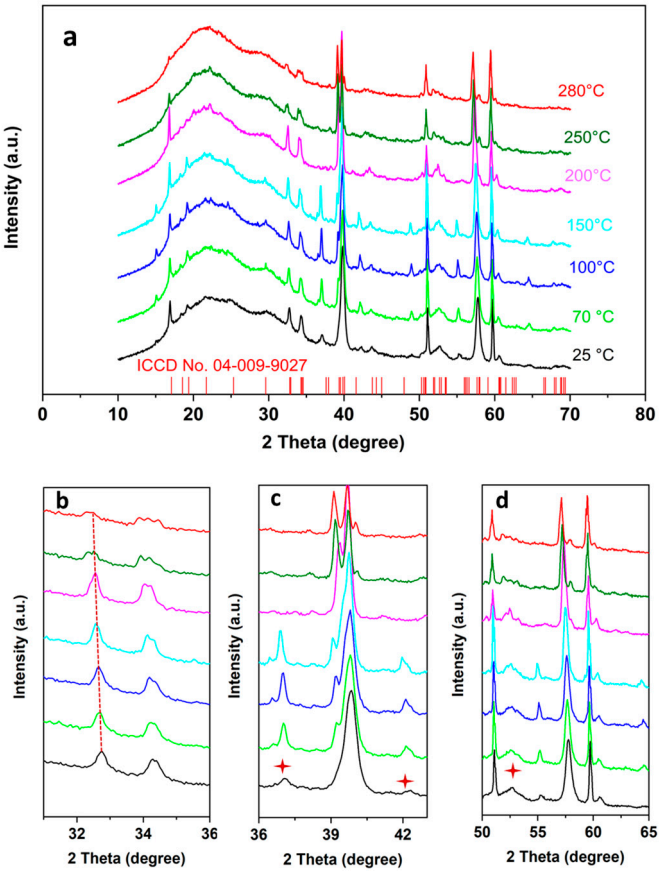

Figure 5. In situ X-ray diffraction patterns of the optimized Li_3InCl_6 electrolyte in the temperature range of 25–280 °C and 10–70 2θ degrees (**a**); Characteristic peaks of the X-ray diffraction patterns in the narrow range of 2θ degrees (**b**–**d**).

To supplement the in situ XRD experiments and provide information about the chemical composition of the Li_3InCl_6 electrolyte surface at different temperatures, in situ/operando high-resolution XPS analysis was performed (Figure 6). In the survey spectrum of Li_3InCl_6 (Figure 6a), the binding energy peak at 198.0 is attributed to Cl 2_p, whereas the peak at 267 eV corresponds to Cl 2s. The In 3d peaks are marked as In $3d_{5/2}$ (444.0 eV) and In $3d_{3/2}$ (451.0 eV). A small presence of surface oxygen could be attributed to the contamination. The Li 1s binding energy is visible at 54.0 eV. Figure 6b–d reveal a slight increase in binding energies with temperature, which could be used to explain potential changes in the chlorine and indium bonding environment. It is necessary to note that the observed effect is opposite to the usually observed slight core-level decrease in binding energies with temperature attributed to increased coulomb repulsion between protons inside the nucleus.

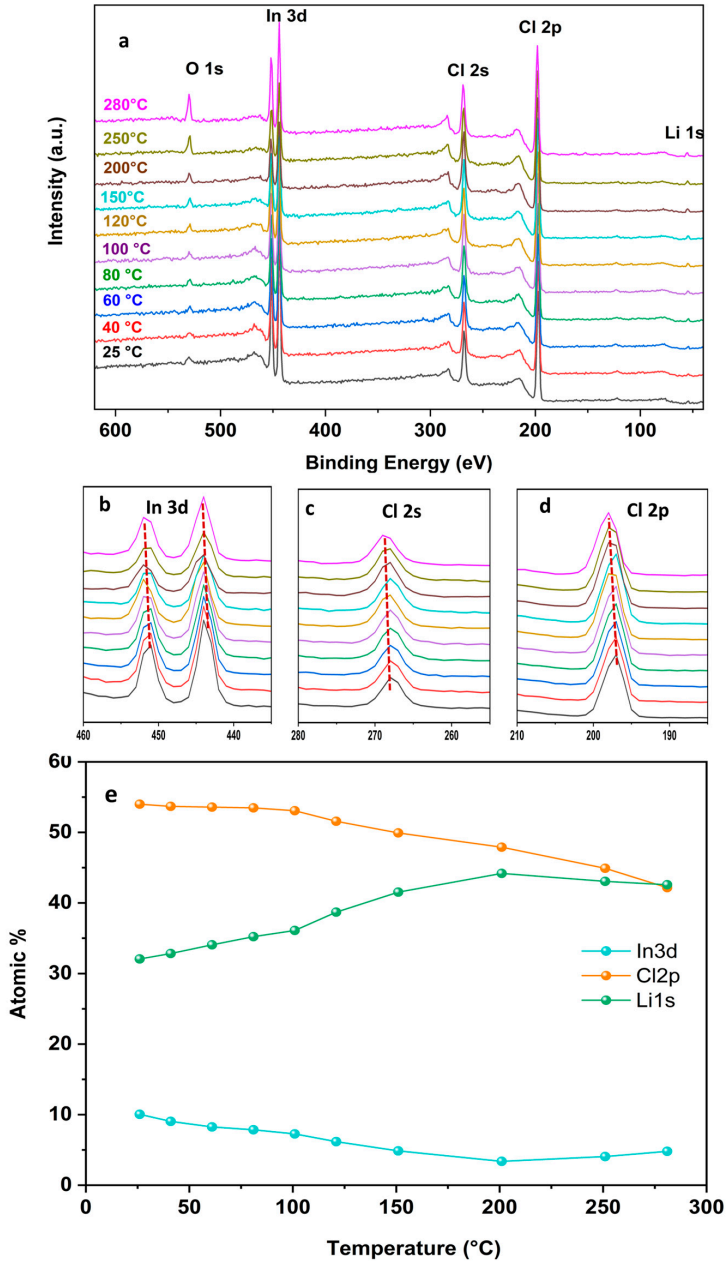

Figure 6. In situ XPS survey spectrum of Li_3InCl_6 at different temperatures (**a**–**c**); atomic percentages of elements with changing temperatures (**d**); Concentrations of indium, chlorine, and lithium on the surface of Li_3InCl_6 at different temperatures (**e**).

The concentrations of lithium, indium, and chlorine on the surface of the Li_3InCl_6 particles were calculated from the corresponding peak intensities (Figure 6e). The indium and chlorine surface concentrations decrease significantly at higher temperatures, while the concentration of lithium gradually increases up to 200 °C. These changes could influence solid-state electrolyte conductivity by affecting ionic transport and contributing to enhanced lithium-ion conductivity.

4. Conclusions

A comprehensive analysis of a lithium halide solid-state electrolyte (Li_3InCl_6) was performed for the first time to gain an understanding of its major trends regarding lithium-ion transport and ionic conductivity in a broad temperature range. The required data were collected through the integration of ex situ and in situ material characterization techniques, such as EIS, TGA/DSC, and in situ X-ray and XPS. Compared to previous publications, the optimized synthesis conditions allowed the production of a Li_3InCl_6 solid-state electrolyte at a lower temperature (260 °C) and shorter ball-milling time. The performed optimization resulted in a high Li_3InCl_6 ionic conductivity of about 1.0 mS cm^{-1} at room temperature. Furthermore, the performed study highlights the enhancement in Li_3InCl_6 ionic conductivity at elevated temperatures that can be ascribed to the corresponding changes in the material's composition, particularly evident from the shifting bonding environments of indium, chlorine, and lithium derived from the in situ XPS measurements.

The TDA/DTS analysis reveals that after the surface-bound water molecules are removed, the mass of Li_3InCl_6 remains constant in the whole temperature range up to 280 °C. However, a negative heat flow was observed that could be assigned to phase transformations in solid-state electrolytes. This assumption is based on previous publications focused on different types of solid-state electrolytes, such as argyrodites or lithium oxyhalides, which can undergo phase transformations from ceramic to glass and glass–ceramic states. When tuning the solid-state electrolyte conductivity at interfaces, the formation of these phases with different mechanisms of ionic transport could be especially important.

The performed in situ XRD and XPS temperature-programmed studies confirm that the structural and chemical changes in Li_3InCl_6 occur, especially at elevated temperatures above 70 °C. The appearance of new peaks in the XRD patterns and changes in the XPS binding energies with temperature indicate that phase transformations take place resulting in different lithium-ion transport mechanisms. It is possible to assume that the changes in the indium and lithium bonding environments could contribute to the observed increase in ionic conductivity above 70 °C. Furthermore, a compression force applied to the powder samples for pellet fabrication and during the electrochemical cell testing is one of the dominant factors in achieving high lithium-ion conductivity. Based on the SEM images and the corresponding impedance data, the absence of porosity in the compressed Li_3InCl_6 samples is particularly important for reaching sufficiently high levels of lithium-ion conductivity at room temperature. The results of this study highlight the importance of different factors in reaching high levels of ionic conductivity and chemical stability for the next-generation lithium-ion and lithium metal batteries, advanced energy storage systems, and environmental sustainability.

Author Contributions: Conceptualization, F.B. and A.W.S.; methodology, F.B.; software, F.B.; validation, F.B. and A.W.S.; formal analysis, F.B.; investigation, F.B. and A.W.S.; resources, F.B. and A.W.S.; data acquisition, F.B., C.R., P.M. and K.L.; writing—original draft preparation, F.B.; writing—review and editing, F.B. and A.W.S.; supervision, A.W.S.; project administration, F.B. and A.W.S.; funding acquisition, A.W.S. All authors have read and agreed to the published version of the manuscript.

Funding: The authors acknowledge financial support from the NSF IUCRC program (Award number 2052631) for supporting the "Center for Solid-state Electric Power Storage (CEPS)" and the South Dakota "Governor's Research Center for Electrochemical Energy Storage" from the South Dakota Board of Regents (Award numbers 442274 and 442385).

Data Availability Statement: The data presented in this study are available on request from the corresponding author.

Acknowledgments: The authors gratefully acknowledge the administrative and technical support from faculty and students at the South Dakota School of Mines and Technology and the colleagues from ThermoFisher Scientific.

Conflicts of Interest: Author Paul Mack was employed by the company Thermo Fisher Scientific. The remaining authors declare that the research was conducted in the absence of any commercial or financial relationships that could be construed as a potential conflict of interest.

References

1. Wang, S.; Wu, Y.; Ma, T.; Chen, L.; Li, H.; Wu, F. Thermal stability between sulfide solid electrolytes and oxide cathode. *ACS Nano* **2022**, *16*, 16158–16176. [CrossRef] [PubMed]
2. Luo, X.; Cai, D.; Wang, X.; Xia, X.; Gu, C.; Tu, J. A novel ethanol-mediated synthesis of superionic halide electrolytes for high-voltage all-solid-state lithium–metal batteries. *ACS Appl. Mater. Interfaces* **2022**, *14*, 29844–29855. [CrossRef] [PubMed]
3. Peng, J.; Wu, D.; Lu, P.; Wang, Z.; Du, Y.; Wu, Y.; Wu, Y.; Yan, W.; Wang, J.; Li, H. High-safety, wide-temperature-range, low-external-pressure and dendrite-free lithium battery with sulfide solid electrolyte. *Energy Storage Mater.* **2023**, *54*, 430–439. [CrossRef]
4. Asano, T.; Sakai, A.; Ouchi, S.; Sakaida, M.; Miyazaki, A.; Hasegawa, S. Solid halide electrolytes with high lithium-ion conductivity for application in 4 V class bulk-type all-solid-state batteries. *Adv. Mater.* **2018**, *30*, 1803075. [CrossRef] [PubMed]
5. Chen, R.; Li, Q.; Yu, X.; Chen, L.; Li, H. Approaching practically accessible solid-state batteries: Stability issues related to solid electrolytes and interfaces. *Chem. Rev.* **2019**, *120*, 6820–6877. [CrossRef] [PubMed]
6. Trahey, L.; Brushett, F.R.; Balsara, N.P.; Ceder, G.; Cheng, L.; Chiang, Y.-M.; Hahn, N.T.; Ingram, B.J.; Minteer, S.D.; Moore, J.S. Energy storage emerging: A perspective from the Joint Center for Energy Storage Research. *Proc. Natl. Acad. Sci. USA* **2020**, *117*, 12550–12557. [CrossRef] [PubMed]
7. Famprikis, T.; Canepa, P.; Dawson, J.A.; Islam, M.S.; Masquelier, C. Fundamentals of inorganic solid-state electrolytes for batteries. *Nat. Mater.* **2019**, *18*, 1278–1291. [CrossRef]
8. Zhu, Y.; Mo, Y. Materials design principles for air-stable lithium/sodium solid electrolytes. *Angew. Chem. Int. Ed.* **2020**, *59*, 17472–17476. [CrossRef]
9. Xu, R.; Wang, X.; Zhang, S.; Xia, Y.; Xia, X.; Wu, J.; Tu, J. Rational coating of Li7P3S11 solid electrolyte on MoS2 electrode for all-solid-state lithium-ion batteries. *J. Power Sources* **2018**, *374*, 107–112. [CrossRef]
10. Auvergniot, J.; Cassel, A.; Ledeuil, J.-B.; Viallet, V.; Seznec, V.; Dedryvère, R. Interface stability of argyrodite Li6PS5Cl toward LiCoO2, LiNi1/3Co1/3Mn1/3O2, and LiMn2O4 in bulk all-solid-state batteries. *Chem. Mater.* **2017**, *29*, 3883–3890. [CrossRef]
11. Wang, D.; Sun, Q.; Luo, J.; Liang, J.; Sun, Y.; Li, R.; Adair, K.; Zhang, L.; Yang, R.; Lu, S. Mitigating the interfacial degradation in cathodes for high-performance oxide-based solid-state lithium batteries. *ACS Appl. Mater. Interfaces* **2019**, *11*, 4954–4961. [CrossRef] [PubMed]
12. Lu, P.; Liu, L.; Wang, S.; Xu, J.; Peng, J.; Yan, W.; Wang, Q.; Li, H.; Chen, L.; Wu, F. Superior all-solid-state batteries enabled by a gas-phase-synthesized sulfide electrolyte with ultrahigh moisture stability and ionic conductivity. *Adv. Mater.* **2021**, *33*, 2100921. [CrossRef] [PubMed]
13. Thangadurai, V.; Narayanan, S.; Pinzaru, D. Garnet-type solid-state fast Li-ion conductors for Li batteries: Critical review. *Chem. Soc. Rev.* **2014**, *43*, 4714–4727. [CrossRef] [PubMed]
14. Sakuma, M.; Suzuki, K.; Hirayama, M.; Kanno, R. Reactions at the electrode/electrolyte interface of all-solid-state lithium batteries incorporating Li–M (M = Sn, Si) alloy electrodes and sulfide-based solid electrolytes. *Solid State Ion.* **2016**, *285*, 101–105. [CrossRef]
15. Li, X.; Liang, J.; Luo, J.; Banis, M.N.; Wang, C.; Li, W.; Deng, S.; Yu, C.; Zhao, F.; Hu, Y. Air-stable Li 3 InCl 6 electrolyte with high voltage compatibility for all-solid-state batteries. *Energy Environ. Sci.* **2019**, *12*, 2665–2671. [CrossRef]
16. Yamada, K.; Matsuyama, S.; Tomita, Y.; Yamane, Y. Lithium-ion conduction mechanism in LiInI4 studied by single crystal 7Li NMR. *Solid State Ion.* **2011**, *189*, 7–12. [CrossRef]
17. Tomita, Y.; Matsushita, H.; Yonekura, H.; Yamauchi, Y.; Yamada, K.; Kobayashi, K. Li ion conductivity of solid electrolyte, Li3−2xMxInBr6 (M = Mg, Ca, Sr, Ba). *Solid State Ion.* **2004**, *174*, 35–39. [CrossRef]
18. Zhou, L.; Zuo, T.-T.; Kwok, C.Y.; Kim, S.Y.; Assoud, A.; Zhang, Q.; Janek, J.; Nazar, L.F. High areal capacity, long cycle life 4 V ceramic all-solid-state Li-ion batteries enabled by chloride solid electrolytes. *Nat. Energy* **2022**, *7*, 83–93. [CrossRef]
19. Li, X.; Liang, J.; Chen, N.; Luo, J.; Adair, K.R.; Wang, C.; Banis, M.N.; Sham, T.K.; Zhang, L.; Zhao, S. Water-mediated synthesis of a superionic halide solid electrolyte. *Angew. Chem.* **2019**, *131*, 16579–16584. [CrossRef]
20. Li, W.; Liang, J.; Li, M.; Adair, K.R.; Li, X.; Hu, Y.; Xiao, Q.; Feng, R.; Li, R.; Zhang, L. Unraveling the origin of moisture stability of halide solid-state electrolytes by in situ and operando synchrotron X-ray analytical techniques. *Chem. Mater.* **2020**, *32*, 7019–7027. [CrossRef]
21. Wang, K.; Ye, Q.; Zhang, J.; Huang, H.; Gan, Y.; He, X.; Zhang, W. Halide electrolyte Li3InCl6-based all-solid-state lithium batteries with slurry-coated LiNi0. 8Co0. 1Mn0. 1O2 composite cathode: Effect of binders. *Front. Mater.* **2021**, *8*, 727617. [CrossRef]

22. Wang, S.; Xu, X.; Cui, C.; Zeng, C.; Liang, J.; Fu, J.; Zhang, R.; Zhai, T.; Li, H. Air sensitivity and degradation evolution of halide solid-state electrolytes upon exposure. *Adv. Funct. Mater.* **2022**, *32*, 2108805. [CrossRef]
23. Liu, Y.; Peng, H.; Su, H.; Zhong, Y.; Wang, X.; Xia, X.; Gu, C.; Tu, J. Ultrafast Synthesis of I-Rich Lithium Argyrodite Glass–Ceramic Electrolyte with High Ionic Conductivity. *Adv. Mater.* **2022**, *34*, 2107346. [CrossRef] [PubMed]
24. Numan-Al-Mobin, A.M.; Schmidt, B.; Lannerd, A.; Viste, M.; Qiao, Q.; Smirnova, A. Interdigitated cathode–electrolyte architectural design for fast-charging lithium metal battery with lithium oxyhalide solid-state electrolyte. *Mater. Adv.* **2022**, *3*, 8947–8957. [CrossRef]
25. Sacci, R.L.; Bennett, T.H.; Drews, A.R.; Anandan, V.; Kirkham, M.J.; Daemen, L.L.; Nanda, J. Phase evolution during lithium–indium halide superionic conductor dehydration. *J. Mater. Chem. A* **2021**, *9*, 990–996. [CrossRef]
26. Song, A.Y.; Xiao, Y.; Turcheniuk, K.; Upadhya, P.; Ramanujapuram, A.; Benson, J.; Magasinski, A.; Olguin, M.; Meda, L.; Borodin, O. Protons enhance conductivities in lithium halide hydroxide/lithium oxyhalide solid electrolytes by forming rotating hydroxy groups. *Adv. Energy Mater.* **2018**, *8*, 1700971. [CrossRef]
27. Molaiyan, P.; Mailhiot, S.E.; Voges, K.; Kantola, A.M.; Hu, T.; Michalowski, P.; Kwade, A.; Telkki, V.-V.; Lassi, U. Investigation of the structure and ionic conductivity of a Li3InCl6 modified by dry room annealing for solid-state Li-ion battery applications. *Mater. Des.* **2023**, *227*, 111690. [CrossRef]